sciendo

Reports on Geodesy and Geoinformatics, 2024, Vol. 118, pp. 82–91

DOI: 10.2478/rgg-2024-0017
Received: 19 April 2024 / Accepted: 3 September 2024
Published online: 6 November 2024

ORIGINAL ARTICLE

Optimized 3D-2D CNN for automatic mineral classification in hyperspectral images

Youcef Attallah [1*], Ehlem Zigh [1] and Ali Pacha Adda [1]

[1]Coding and Security of Information Laboratory (LACOSI), Department of Electronics, Faculty of Electrical Engineering, University of Science and Technology of Oran Mohamed-Boudiaf (USTOMB), 31000, Oran, Algeria

*youcef.attallah@univ-usto.dz

Abstract

Mineral classification using hyperspectral imaging represents an essential field of research improving the understanding of geological compositions. This study presents an advanced methodology that uses an optimized 3D-2D CNN model for automatic mineral identification and classification. Our approach includes such crucial steps as using the Diagnostic Absorption Band (DAB) selection technique to selectively extract bands that contain the absorption features of minerals for classification in the Cuprite zone. Focusing on the Cuprite dataset, our study successfully identified the following minerals: alunite, calcite, chalcedony, halloysite, kaolinite, montmorillonite, muscovite, and nontronite. The Cuprite dataset results with an overall accuracy rate of 95.73 % underscore the effectiveness of our approach and a significant improvement over the benchmarks established by related studies. Specifically, ASMLP achieved a 94.67 % accuracy rate, followed by 3D CNN at 93.86 %, SAI-MLP at 91.03 %, RNN at 89.09 %, SPE-MLP at 85.53 %, and SAM at 83.31 %. Beyond the precise identification of specific minerals, our methodology proves its versatility for broader applications in hyperspectral image analysis. The optimized 3D-2D CNN model excels in terms of mineral identification and sets a new standard for robust feature extraction and classification.

Key words: hyperspectral imaging, mineral identification, Optimized 3D-2D CNN, diagnostic absorption band, feature extraction

1 Introduction

Hyperspectral imaging has become increasingly important in the past few decades in various remote sensing applications, including mineral exploration, environmental monitoring, and agriculture. One of its main applications is mineral identification, where distinctive spectral signatures, which depend on chemical composition and crystal structure, are examined for classification purposes (Dennison et al., 2004). Hyperspectral imaging offers significant advantages in mineral identification by providing a more detailed spectral information as compared with multispectral or monospectral imaging techniques. This capability facilitates the discrimination of minerals with similar spectral signatures. In addition, hyperspectral imaging allows us to identify minerals in poorly lit, heavily vegetated or isolated areas and distinguish minerals mixed with or hidden in other materials (Chakraborty et al., 2022).

Researchers have previously explored the classification of minerals in hyperspectral images using several traditional methods. Alongside the Spectral Angle Mapper (SAM) (Yuhas et al., 1992), Spectral Information Divergence (SID) (Chang, 1999), the Spectral Correlation Mapper (SCM) (De Carvalho and Meneses, 2000), other methodologies, including the Bayesian Classifier (Langley et al., 1992), K-means Classification (El Rahman, 2016), and Spectral Indices (Kumar et al., 2015), have undergone a thorough examination. SAM quantifies the spectral angle between the pixel spectral signatures (Tripathi and Govil, 2019), SID measures informational divergence, and SCM is based on spectral correlation (Li and Niu, 2015). The Bayesian Classifier uses conditional probabilities for classification (Kozoderov et al., 2015), K-means Classification is based on spectral signature similarity (Ranjan et al., 2017), and Spectral Indices employ specific band ratios (Mahlein et al., 2013). While these traditional techniques have proven effective in extracting distinctive spectral features from minerals, it is paramount to acknowledge their specific limitations: Notably, these methods encounter challenges when confronted with the inherent complexity of hyperspectral data and distinguishing minerals with similar

This work is available in Open Access model and licensed under a Creative Commons Attribution-NonCommercial-NoDerivatives 4.0 License.
Publisher: De Gruyter

spectral signatures. In addition to these challenges, the scarcity of labeled samples poses a significant obstacle to training deep learning models for mineral identification and classification (Rao et al., 2019). 2019). To address these issues, we propose an integration of the diagnostic Diagnostic Absorption Band (DAB) selection technique to select and extract bands that contain the absorption characteristics of the minerals selected for classification in the Cuprite area. This method, specifically, allows us to target spectral bands where the absorption characteristics of the minerals are most pronounced, facilitating their distinction and precise identification in hyperspectral data. Moreover, by reducing the spectral dimensions, we simplify the complexity of the data while preserving the essential information necessary to extract robust features for classification. In this way this approach improves the performance and reliability of deep learning models for hyperspectral image analysis in mineral classification Hecker et al. (2019).

Deep learning has become the current approach to Hyperspectral Image Categorization (HSI) as it can independently capture hierarchical features, ranging from basic to complex, directly from hyperspectral data. These captured features have proven highly effective in a number of visual industrial missions. However, despite the widespread application of deep learning to remote sensing and hyperspectral image analysis, most studies have focused mainly on urban, landscape, and vegetation categories, using data sets such as: the Pavia University, the Salinas scene, and Indian pines. In particular, research on mineral classification is still rare and limited.

Mou et al. (2017) used Recurrent Neural Networks (RNN) to classify hyperspectral images accurately. Their RNN model was specifically designed to process the sequential hyperspectral pixel data and incorporated a new activation function, PRetanh, which significantly improved the data processing capabilities (Mou et al., 2017). Regarding the application of mineral classification based on hyperspectral images, (Deng et al., 2021) have introduced a method for classifying minerals in hyperspectral images based on the Attenuation Spectral Absorption Index (ASAI) to extract absorption characteristics from diagnostic mineral bands. These features are integrated to construct an ASAI vector and are subsequently applied to develop a Multilayer Neural Network (MLP) model for mineral identification. While this approach focuses primarily on spectral absorption attributes, it neglects explicit considerations of the spatial complexities inherent in hyperspectral data (Deng et al., 2021).

Convolutional Neural Networks (CNNs) have garnered considerable praise for their effectiveness in feature extraction due to their inherent capacity to learn hierarchical representations from raw data. It is essential to clarify the roles of the different types of CNN in this context. A 1D CNN is designed to process one-dimensional data, such as time series, audio signals, or sequences where information is ordered along a single dimension (Ige and Sibiya, 2024). 2D CNNs excel at spatial feature extraction thanks to their ability to process two-dimensional data, such as images (Kong et al., 2022). Meanwhile, 3D CNNs have a superior ability to extract spectral features compared to 1D and 2D CNNs (Ma et al., 2023). In the mineral identification process, the robustness of CNNs is demonstrated by their ability to capture complex spectral patterns for distinguishing different minerals (Ozdemir and Polat, 2020). This prowess is particularly notable when considering the architecture of CNNs, which comprises 3D and 2D convolutional layers. 3D convolutional layers play a crucial role in hyperspectral data processing, as they are designed to address the extra spectral dimension present in hyperspectral images. These layers can effectively capture the nuanced spectral characteristics specific to different minerals by analyzing spectral information at multiple wavelengths simultaneously, thus enhancing the model's discrimination capabilities. Meanwhile, 2D convolutional layers complement 3D convolutional layers by focusing on capturing spatial information in the given image. They analyze the spatial relationships between neighboring pixels, enabling the model to discern features and structures that help identify mineral types according to their SpectroSpatial relationships. This information is essential for accurate mineral identification, especially in cases where minerals have similar spectral signatures but differ in spatial distribution or arrangement (Fırat et al., 2022).

Zhang et al. (2022) proposed the application of deep learning methodologies for mineral classification in hyperspectral remote sensing data by developing and evaluating three distinct neural network architectures, including a hybrid 1D and 2D CNN. 1D neural networks can hardly capture spectral information as they are limited in terms of integrating spatial-contextual information. These limitations highlight the importance of using more complex architectures, such as 2D or 3D neural networks, which can exploit inherent spatial and spectral features more effectively, thereby improving the classification performance (Zhang et al., 2022). Regarding the application of 3D and 2D convolution neural networks, citet28 proposed the hybridSN architecture, which uses spatial and spectral information in addition to 3D and 2D convolutions, which is superior to recent urban and vegetation classification approaches, as confirmed by experiments on three standard datasets. In addition, the hybrid SN model offers superior computational efficiency and achieves high performance, regardless of limited training data (Roy et al., 2019). Ghaderizadeh et al. (2021) presented a novel approach proposing a hybrid 3D and 2D convolution model for urban and vegetation classification of Hyperspectral Images (HSI). Their architecture exploits spatial and spectral features to improve classification performance obtained from 3D and 2D convolutions. This combination of 3D and 2D CNN reduces the number of training parameters and is less computationally complex (Ghaderizadeh et al., 2021).

Our research introduces a new approachan innovative approach to mineral identification in hyperspectral images by proposing a hybrid 3D-2D CNN architecture optimized for automatic mineral classification. In hyperspectral imaging, 2D CNNs and 3D CNNs are often used together to take advantage of their ability to combine spatial and spectral features. Specifically, the 3D CNN extracts selected spatial features, which the 2D CNN then refines. This complementary relationship between the 3D and 2D CNNs allows for a complete extraction of the spatial and spectral features of each pixel, as observed in several studies, such as those by Roy et al. (2019) and Ghaderizadeh et al. (2021). In general, the 3D-2D CNN combination is often considered the most effective approach for identifying and classifying hyperspectral images due to its ability to capture spectral features (each pixel containing a rich spectral signature) and spatial features (patterns and structures visible across spectral bands). It fully exploits the potential of hyperspectral data, considering the complex relationships between spectral and spatial information, and holds a promise for the future of mineral classification.

Unlike previous studies, which mainly focused on hybrid architectures for urban and vegetation classification, our innovative approach applies these hybrid models for the first time in mineral classification. A careful integration of spectral and spatial information, enables our hybrid CNN model to identify minerals more accurately, with significantly higher efficiency which outperforms traditional methods and previous studies in this field. In addition, our optimized hybrid model substantially reduces the number of parameters to be trained as compared to the existing 3D-2D CNN models while maintaining comparable performance. This superior efficiency makes our model a practical and cost-effective solution for mineral classification in hyperspectral images. By refining several hyperparameters and optimizing the model architecture, we aim to improve the accuracy of mineral classification in hyperspectral images further.

The following sections of our study are structured to provide a comprehensive explanation of our approach. Section 2 details the materials and methods and offers an overview of our optimized 3D-2D CNN hybrid architecture. Section 3 presents an in-depth analysis of the results, comparing our optimized 3D-2D CNN with existing

approaches to highlight its superiority in mineral classification tasks. Finally, Section 4 concludes our study by summarizing the main results and proposing directions for future research.

2 Materials and methods

2.1 Diagnostic Absorption Bands selection

Hyperspectral images contain large volumes of spectral data, with some bands potentially redundant or containing only minimal information relevant for mineral classification (Peyghambari and Zhang, 2021). Mineral classification in hyperspectral images has been a significant challenge in geology and earth sciences (Van der Meer et al., 2012). These images capture detailed spectral information, allowing us to identify minerals based on their unique light absorption properties (Laukamp et al., 2021). Different minerals exhibit distinct absorption bands in their spectra, acting as fingerprints (Figure 1). Analyzing these spectral signatures allows us to distinguish different types of minerals (Beiswenger et al., 2018).

DAB selection method focuses on identifying specific absorption features in the spectral signature of minerals. Each mineral exhibits unique absorption characteristics at particular wavelengths, which are diagnostic criteria to differentiate it from other minerals (Table 1).

In our study, the DAB technique was implemented using ENVI software, a powerful tool for hyperspectral image analysis (Xing and Gomez, 2001). The process begins with the analysis of the central absorption frequencies of each mineral, as illustrated in Figure 1 and summarized in Table 1. After selecting the relevant diagnostic absorption bands for each mineral class, the other spectral bands were removed, leaving only the critical bands that provide the necessary information for accurate mineral identification. This process significantly reduces the dimensionality of the data, which has the following advantages:

- *Improved Classification Efficiency:* by focusing on the most relevant spectral information, the DAB selection method streamlines the feature extraction and classification process, which translates into shorter processing times and lower computational costs.
- *Enhanced Feature Extraction:* with fewer and more informative bands, feature extraction algorithms can operate more effectively. This allows for the extraction of more robust and discriminative features that accurately represent the unique spectral properties of each mineral accurately.
- *Reduced Noise Sensitivity:* hyperspectral data can be susceptible to noise from various sources. By selecting only the most informative bands, the DAB method helps mitigate the impact of noise on the classification process, leading to more reliable results.
- *Interpretability:* focusing on a smaller set of diagnostic bands can enhance the interpretability of the classification results. By understanding which bands contribute most to the classification of a particular mineral, geologists can gain valuable insights into the mineral composition of the study area.

Figure 1 illustrates the spectral signatures of these minerals, highlighting their unique absorption frequencies. Additionally, Table 1 summarizes the diagnostic band characteristics for each mineral. After implementing the DAB selection method, the spectral dimension of our hyperspectral image is reduced to a compact set of nine crucial diagnostic bands. This reduction in spectral dimension, achieved by the DAB method, simplifies the data while increasing its informative value. It provides a solid basis for feature extraction and the subsequent classification of minerals in the hyperspectral image. The resulting DAB vector is formulated as follows:

Table 1. Spectral characteristics of identified minerals

Mineral Class	Diagnostic Bands (nm)
Alunite	2170–2320
Calcite	2160–2340
Chalcedony	2250
Halloysite	2170–2210
Kaolinite	2170–2210
Montmorillonite	2210
Muscovite	2200–2350
Nontronite	2290

$$DAB = [B_{2160},\ B_{2170},\ B_{2200},\ B_{2210},\ B_{2250},\ B_{2290},\ B_{2320},\ B_{2340},\ B_{2350}]. \quad (1)$$

Our study focuses on eight mineral classes: alunite, calcite, chalcedony, halloysite, kaolinite, montmorillonite, muscovite, and nontronite. The selection was motivated by these factors:
Firstly, it was essential to ensure a sufficient number of formation and test samples for a robust assessment of model performance while avoiding mixed pixels due to limitations in spatial resolution and mineralization effects. The wide distribution of the mineral classes in the Nevada Cuprite mining area allowed for their selection (Figure 3).
Additionally, we selected only these classes to facilitate direct comparisons with other studies, which commonly use seven mineral classes: alunite, calcite, chalcedony, halloysite, kaolinite, montmorillonite, and muscovite (Deng et al., 2021). We included the nontronite class because of its specific absorption characteristics in the chosen spectral range (2000 to 2500 nm) and its large pixel area, making it a particularly useful representation for our analysis.

2.2 Convolutional Neural Network

Recently, a number of new deep learning methodologies applied to classification have been developed. CNNs have been emerging as leading architectures in this landscape. These networks consist of several layers, including convolutional, pooling, and fully connected layers, using specific mathematical operations to extract and analyze relevant features from input data (Gu et al., 2018; Bhatt et al., 2021). The pooling layer plays a crucial role in reducing the spatial dimension of the feature map, while the fully connected layer, adopting a multilayered perceptron approach, connects all neurons to succeeding layers. The output characteristics of the latter layer allow the characteristics to correspond with the output. Mathematically, the output of input X corresponds to the following:

$$Y = \omega(W \times X + B). \quad (2)$$

Here, Y represents the output, W denotes the weight, B signifies the bias, and the function $\omega(.)$ corresponds to the nonlinear activation applied to a weighted sum of inputs, where the ReLU activation function is used in this section and can be expressed as follows:

$$ReLU(x) = \begin{cases} x, & \text{if } x > 0; \\ 0, & \text{if } x \leq 0. \end{cases} \quad (3)$$

The use of the ReLU function has the following advantages: Firstly, the constant derivative associated with positive values increases the learning speed of the network. Secondly, the network layers extract features useful for the final classification (Ghaderizadeh et al., 2021).

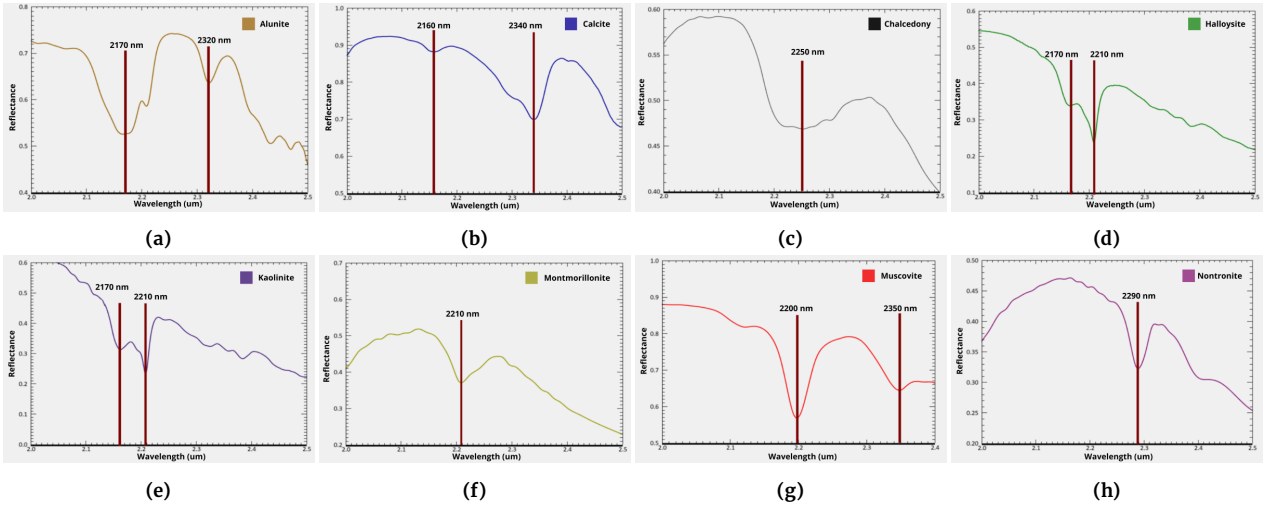

Figure 1. Mineral diagnostic signatures – unveiling absorption frequencies: (a) Alunite, (b) Calcite, (c) Chalcedony, (d) Halloysite, (e) Kaolinite, (f) Montmorillonite, (g) Muscovite, (h) Nontronite.

Our 3D-2D-CNN model comprises three distinct stages:

- *Patch extraction:* selects small samples around each image pixel.
- *Feature extraction:* a deep learning model analyzes patches to extract discriminating features.
- *Label identification:* each pixel is classified according to the characteristics of its corresponding patch.

Pooling layers have been removed from all three models to maximize the amount of usable information. Consider our HSI as a cube with width (W), height (L), and depth (H) representing the number of spectral bands. After selecting the most informative bands (diagnostic bands, DAB), we obtain an input image I_p of dimensions ($W \times L \times B$), where B is the number of selected bands. We aim to predict the class (label) for each pixel. The first step in the patch extraction is to create patches around each pixel. The size of these patches ($P \times P \times B$) depends on the center of the individual pixels. Since pixels near the edges of the image may not contain enough data to create the desired patch size, we use a fill operation to add additional information, creating a "background" for these edge pixels. The position of each pixel in the image is (x, y). The total number of patches generated is calculated as follows:

$$N_p = (W - (P + 1)) \times (L - (P + 1)). \quad (4)$$

Therefore, the entry of the patch I_p will be expressed as $I_p^{(x,y)}$ and covers a length between $x - (p - 1)/2$ and $x + (p - 1)/2$ and a width between $y - (p - 1)/2$ and $y + (p - 1)/2$. Each patch extracted using multiple channels is processed separately as an image. The deep CNN model with 2-D convolution layers extracts feature maps for the patches. The operating formula for the 2-D CNN in each layer is as follows:

$$Y_{l,f}^{\alpha,\beta} = f\left(\sum_{F_m}\sum_{j=0}^{Y}\sum_{i=0}^{X} W_{l,f,F_m}^{i,j} \otimes X_{\alpha+i,\beta+j}^{l-1,F_m} + b^{l,f}\right). \quad (5)$$

In the context of a 2D-CNN network, l is the processed layer, and f is the feature map of layer l. Variables (α, β) indicate the position in the patch, while (x, y) represent the position of the kernel in the feature map f of layer l. F_m represents the total number of input feature maps in the neuron, while (i, j) indicates the position of the convolution filter on the feature map f of layer l. The 3D-CNN model includes an additional spectral band sorting step, which is absent from the 2D-CNN model. The sorting orders images of similar spectral bands into sequences, preserving their spectral correlations. Both models share the same patch extraction and label recognition steps. Feature extraction in the 3D-CNN model uses a 3D convolution operator, unlike 2D-CNN, which applies a 2D convolution operator (Ghaderizadeh et al., 2021). The 3D convolution formula is given below:

$$Y_{l,f}^{\alpha,\beta,\gamma} = f\left(\sum_{F_m}\sum_{k=0}^{Z}\sum_{j=0}^{Y}\sum_{i=0}^{X} W_{l,f,F_m}^{i,j,k} \otimes X_{\alpha+i,\beta+j,\gamma+k}^{l-1,F_m} + b^{l,f}\right). \quad (6)$$

The patch has a specific size (X, Y, Z), encompassing both spatial dimensions (width and height) and spectral dimensions (number of bands). Each data point on the patch is identified by its spatial coordinates (α, β) and spectral band (γ). Similarly, during convolution, the filter's position in a feature map is denoted by (i, j, k), where i and j represent its spatial position, and k indicates the specific spectral band over which the filter operates in the feature map.

2.3 Our proposed 3D-2D CNN

This study introduces our optimized hybrid CNN architecture for mineral classification from hyperspectral images. Our approach leverages a 3D-2D CNN specifically designed to exploit spatial and spectral information present in these complex images. As illustrated in Figure 2, our optimized architecture comprises four 3D convolution layers designed to capture specific spatial and spectral features of the hyperspectral image data.

The kernel sizes used in these 3D layers are defined as $8 \times 3 \times 3 \times 7 \times 1$ (i.e., $F_1^1 = 3, F_2^1 = 3$ and $F_3^1 = 7$), $16 \times 3 \times 3 \times 5 \times 8$ (i.e., $F_1^2 = 3, F_2^2 = 3$ and $F_3^2 = 5$), $16 \times 3 \times 3 \times 3 \times 16$ (i.e., $F_1^3 = 3, F_2^3 = 3$ and $F_3^3 = 3$), and $32 \times 3 \times 3 \times 3 \times 16$ (i.e., $F_1^4 = 3, F_2^4 = 3$ and $F_3^4 = 3$) for the four layers, respectively. As an example, the size $16 \times 3 \times 3 \times 5 \times 8$ indicates the use of 16 3D convolution kernels of dimension $3 \times 3 \times 5$ for each of the 8^{th} input feature maps. The 2D section of our model consists of three 2D convolution layers. These are, respectively, $128 \times 3 \times 3 \times 32$ (that is, $F_1^1 = 3$ and $F_2^1 = 3$), $64 \times 3 \times 3 \times 128$ (that is, $F_1^2 = 3$ and $F_2^2 = 3$) and $32 \times 3 \times 3 \times 64$ (that is, $F_1^3 = 3$ and $F_2^3 = 3$). The size of $64 \times 3 \times 3 \times 128$ corresponds to 64 2D convolution filters of size 3×3, with 128 output feature maps.

Finally, by flattening the output of the seventh layer, all neurons are connected to those in the subsequent layer, which comprises 256 neurons, followed by a layer of size 128, and ultimately culminating in the last classification layer with a total of 8 mineral classes. Table 2 provides an overview of the proposed model regarding layer types, output map dimensions, and parameter counts. In particular, the maximum number of parameters reside in the initial dense

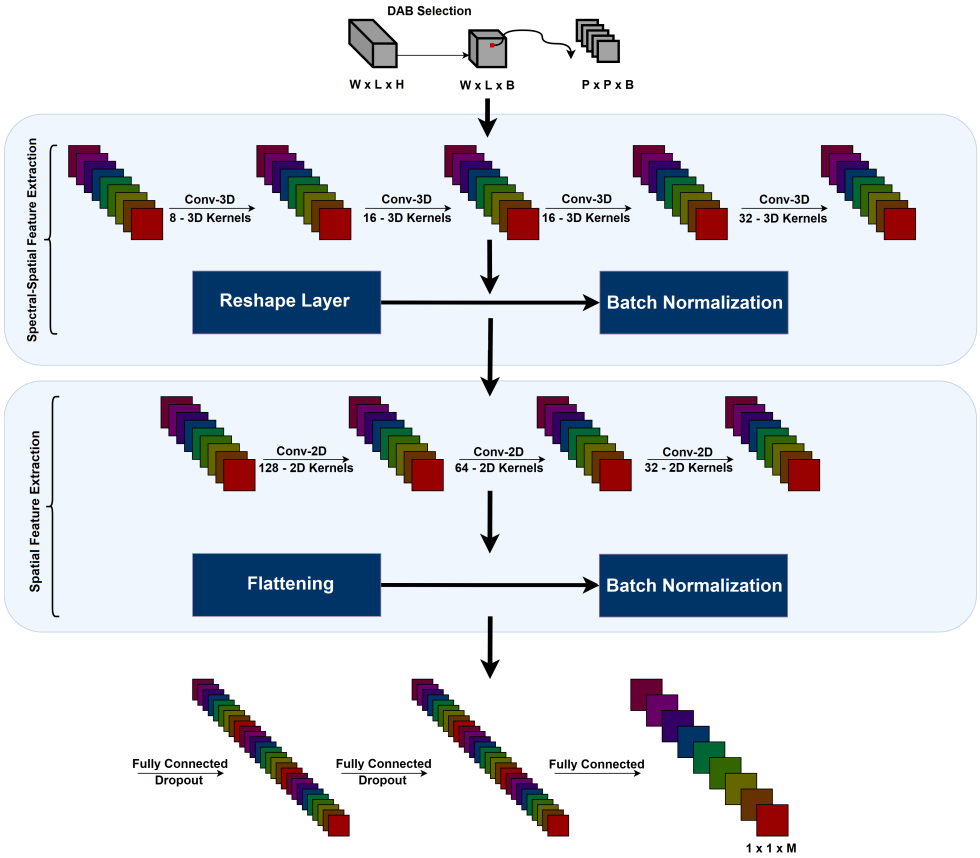

Figure 2. Proposed work (architecture of our Optimized 3D-2D CNN for mineral classification)

(fully connected) layer. Consequently, the proposed model's total number of parameters depends on the number of classes within the data set. For the Cuprite dataset, the total count of trainable weight parameters in the proposed model amounts to 648,232. All weights are randomly initialized and then refined using the backpropagation algorithm with the Adam optimizer and Softmax activation for classification. We configured our networks to 100 epochs and mini-batches of 256 samples (Batchsize), with a learning rate set at 0.001 without data augmentation. This design enables our hybrid CNN network to efficiently capture spatial and spectral information from hyperspectral images, using 3D convolutions to exploit the spectral richness of the data and 2D convolutions to extract finer spatial features.

2.4 Experimental settings

Dataset description and training configuration

Located in Nevada, the Cuprite mine offers a unique field of study due to its abundant mineral deposits. The hyperspectral data set acquired by the AVIRIS sensor in the area provides a valuable tool for mineral identification research. Covering an area of 400×350 pixels and containing 50 near-infrared bands, this data set enables exploration of the spectral properties of various minerals (Swayze et al., 2014). By employing advanced deep learning methods, researchers can now confirm the mineral composition of the region with an unprecedented level of precision, instilling confidence in the accuracy of our findings. Exploiting this database paves the way for new applications in mining exploration and natural resource management. A comprehensive understanding of the mineral distribution in the Cuprite region will help optimize resource extraction and minimize the environmental impact of mining activities. Further details, including a false color image and a ground truth map, are

Table 2. Summary of our optimized 3D-2D CNN architecture

Layer (Type)	Output shape	Parameters
Input Layer	(25, 25, 9, 1)	0
Conv3D 1 (Conv3D)	(19, 23, 7, 8)	512
Conv3D 2 (Conv3D)	(15, 21, 5, 16)	5776
Conv3D 3 (Conv3D)	(13, 19, 3, 16)	6928
Conv3D 4 (Conv3D)	(11, 17, 1, 32)	13856
Reshape 1 (Reshape)	(11, 17, 32)	0
Batch Normalization 1	(11, 17, 32)	128
Conv2D 1 (Conv2D)	(9, 15, 128)	36992
Conv2D 2 (Conv2D)	(7, 13, 64)	73792
Conv2D 3 (Conv2D)	(5, 11, 32)	18464
Flatten (Flatten)	(1760)	0
Batch Normalization 2	(1760)	7040
Dropout 1 (Dropout)	(1760)	0
Dense 1 (Dense)	(256)	450816
Dropout 2 (Dropout)	(256)	0
Dense 2 (Dense)	(128)	32896
Dropout 3 (Dropout)	(128)	0
Dense 3 (Dense)	(8)	1032
Total Parameters		648232

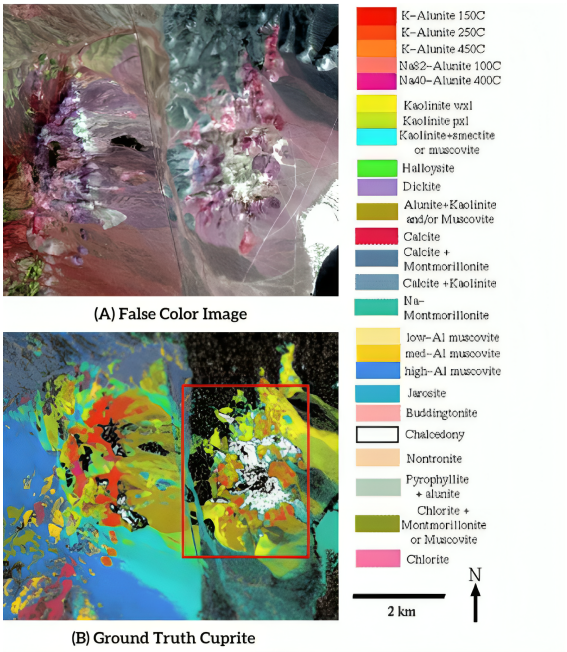

Figure 3. Ground truth and false color image of the cuprite dataset

available in Figure 3 for visualization.

Our computing infrastructure, based on an Intel Core i7-12700F processor coupled with 64 GB of memory, formed the basis of our experimental work. Furthermore, to ensure our results' optimal efficiency and reproducibility, we exploited the computing performance of a GeForce RTX 3070 Ti GPU.

We normalized the spatial dimensions by extracting 3D patches of size $25 \times 25 \times 9$ for all previous methods. Each patch was processed independently as an image, with the central pixel representing the target mineral class, ensuring efficient training and extraction of spatial and spectral features. The dataset was randomly partitioned into 70% for training, 10% for validation, and 20% for testing. To maintain balance across all mineral classes, we selected a total of 650 samples per class: 500 samples for training (70%), 50 samples for validation (10%), and 100 samples for testing (20%). We carefully ensured that image patches did not overlap, preventing any information leakage between the training and testing sets. This step is crucial to maintain the independence of the test data and avoid any bias in the model evaluation.

Optimization methods

Overfitting in hyperspectral mineral classification limits the ability of CNN models to classify unpublished data. Our methodology addresses this challenge by incorporating optimization techniques as: batch normalization, L2 regularization, learning rate decay, dropout, and K-fold cross-validation. These techniques improve learning stability collectively and promote superior model generalization for robust classification performance.

- *Regularization:* We specifically focus on integrating L1 and L2 regularization methods into our 3D-2D CNN architectures. L1 regularization promotes the selection of characteristics by penalizing the absolute values of the network weights. In contrast, L2 regularization stabilizes the model by penalizing the squared magnitudes of the weights, reducing the risk of overfitting and improving generalization to new data (Farhadi et al., 2022). After careful hyperparameter tuning, we selected regularization strengths of 0.006 for L1 and 0.016 for L2. By incorporating these techniques, we aim to balance model complexity and generalization capacity, ultimately facilitating precise and robust mineral classification in hyperspectral imagery, as demonstrated on the Cuprtie dataset.
- *Batch Normalization:* To improve training stability and convergence, we meticulously integrated batch normalization into our 3D-2D CNN architecture, employing a configuration with a momentum of 0.99 and an epsilon of 0.001. This technique normalizes activations between layers, reducing internal variations and accelerating the learning. By maintaining consistent input throughout the network, batch normalization helps avoid vanishing or exploding gradients, leading to smoother optimization (Jung et al., 2019). This approach balances model complexity with generalization for robust mineral classification in hyperspectral images.
- *Dropout:* Dropout regularization has been seamlessly incorporated into our 3D-2D CNN architectures to enhance model robustness and mitigate overfitting. During training, this regularization technique randomly deactivates a quarter (25%) of neurons in each layer. By discouraging interdependencies between neurons, dropout encourages the network to learn more independent features, enhancing generalization and reducing over-fitting (Wu and Gu, 2015).
- *Learning Rate Decay:* We applied learning rate decay, setting it to a value of 1e-07. This strategy ensures that the learning rate gradually decreases during training, enabling the model to converge more efficiently toward an optimal solution.
- *K-Fold Cross Validation:* Finally, we used the K-Fold cross-validation technique, subdividing our dataset into four folds ($K = 4$). This approach enabled full validation of the performance of our model, which was trained and evaluated on several subsets of data. By systematically going through different combinations of training and validation sets, we obtained a comprehensive assessment of our model's generalizability. Through the meticulous application of K-Fold cross-validation, we prepared to validate the robustness and reliability of our mineral classification model.

Our study replicated all experiments under identical conditions to ensure fair comparisons, including consistent data preprocessing steps such as normalization and data splitting. By maintaining uniform hyperparameters across different methods, we ensured the comparability of results. The selected hyperparameters, summarized in Table 3, were tuned based on preliminary experiments to optimize performance while maintaining fairness and consistency across methods.

3 Results and discussion

3.1 Evaluation metrics

In our study, we used various measures to evaluate the performance of our classification approach. In addition to assessing overall model accuracy (OA), we used the Kappa coefficient to measure the agreement between predicted and actual classifications, which provides a comprehensive assessment considering the chance agreement. In addition, we calculated average accuracy (AA) to provide class-specific assessments, revealing potential performance gaps between different classes (Story and Congalton, 1986; McHugh, 2012). These complementary evaluation measures have enabled us to gain a better understanding of the capabilities and limitations of our classification model, as shown in the following equations:

$$OA = \frac{(TP + TN)}{(TP + TN + FP + FN)}, \tag{7}$$

$$Kappa = \frac{P_0 - P_e}{1 - P_e}, \tag{8}$$

Table 3. Hyperparameters used for comparisons

Method	Parameter	Value
SAM	Maximum Angle (radians)	0.1
SPE-MLP SAI-MLP ASMLP	Hidden Layers Sizes	100
	Solver	Adam
	Batch Size	256
	Learning Rate	0.001
	Activation Function	ReLU
	Max Iterations	1000
3D-CNN 3D-2D CNN RNN	Activation Function	ReLU
	Epochs	100
	Batch Size	256
	Optimizer	Adam
	Loss Function	Categorical Crossentropy
	Learning Rate	0.001
	Regularization (L1)	0.006
	Regularization (L2)	0.016
	Momentum	0.99
	Epsilon	0.001
	Dropout	25%
	Learning Rate Decay	10^{-7}
	K-Fold	4
	Number of Units (RNN)	128
	Number of Layers (RNN)	3
	Type of RNN Used	LSTM

$$AA = \left(\frac{1}{N}\right) \times \sum_{i=0}^{i=n} \frac{TP_i}{TP_i + FP_i}, \tag{9}$$

where:

- TP is the number of true positives,
- TN is the number of true negatives,
- FP is the number of false positives,
- FN is the number of false negatives,
- P_0 is the observed agreement,
- P_e is the expected agreement by chance.

In addition, we have integrated the F1-Score, recall, and precision measures into our evaluation, thus obtaining a better understanding of the model's performance in various aspects. These evaluation measures are listed below:

$$\text{Precision} = \frac{TP}{(TP + FP)}, \tag{10}$$

$$\text{Recall} = \frac{TP}{(TP + FN)}, \tag{11}$$

$$\text{F1-Score} = \frac{2 \times \text{Precision} \times \text{Recall}}{\text{Precision} + \text{Recall}}. \tag{12}$$

3.2 Classification rResults

In this section, we present the mineral classification results of our optimized 3D-2D convolutional neural network (CNN) model for the classes: Alunite, Calcite, Chalcedony, Halloysite, Kaolinite, Montmorillonite, Muscovite, Nontronite. Figure 4 illustrates the learning curves of our model, showing its performance in terms of accuracy and loss over the learning periods. The model performs remarkably well during the learning process, achieving an accuracy of 99.43%. This high accuracy underlines the effectiveness of the proposed approach in accurately classifying minerals from hyperspectral data.

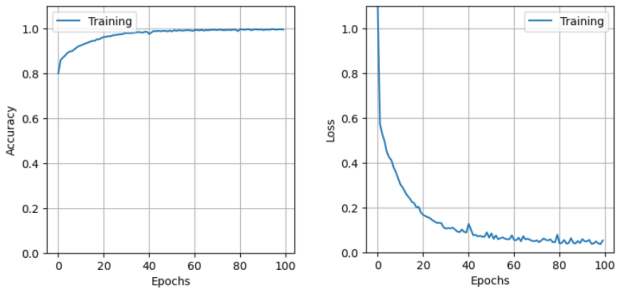

Figure 4. Learning curves of Optimized 3D-2D CNN for mineral classification

Table 4. Detailed mineral classification results using our Optimized 3D-2D CNN

Classes	Precision	Recall	F1-Score
Alunite	0.95	0.97	0.96
Calcite	0.97	0.96	0.97
Chalcedony	0.94	0.95	0.95
Halloysite	0.94	0.94	0.95
Kaolinite	0.92	0.91	0.92
Montmorillonite	0.93	0.93	0.94
Muscovite	0.98	0.98	0.98
Nontronite	0.93	0.94	0.93
Average	0.95	0.94	0.95
Overall Accuracy		0.9573	
Average Accuracy		0.9508	
Kappa		0.9481	

Furthermore, the loss function shows a steady decrease over the epochs, reaching a minimum value of 0.0730 after 100 epochs. This downward trend indicates that the model learns efficiently from the training data, minimizes errors, and improves its predictive capacity. These results validate the effectiveness of our optimized CNN architecture in achieving outstanding performance in mineral classification tasks, highlighting its potential for practical applications in mineralogy and remote sensing.

The results presented in Table 4 give a detailed overview of the performance of our classification model for eight mineral classes in the cuprite zone. Each mineral class shows high accuracy values, between 93% and 95%, indicating our model's high performance in mineral classification. This level of accuracy guarantees the reliability of the model's predictions, which is crucial for applications requiring accurate mineral classification. It is worth noting that the recall values for all mineral classes are high, ranging from 91% to 98%. This recall rate underscores the model's effectiveness in capturing the majority of instances belonging to each mineral class, a crucial factor for comprehensive mineral mapping and analysis tasks. The combination of high precision and recall further highlights the robustness of our model in accurately identifying mineral occurrences within hyperspectral data.

The F1 scores for each mineral class, all above 92%, reflect a harmonious balance between precision and recall. Achieving precisely balanced recall is crucial to ensuring the model's predictions are accurate and complete, particularly in scenarios where FP or FN can have significant consequences. The general evaluation of our model reveals a remarkable performance in mineral classification using the cuprite dataset. The overall accuracy is 95. 73%, with an average precision of 95. 08% and the Kappa coefficient of 94.81% for all mineral classes confirm the consistency and reliability of our approach. These significant results underline the usefulness of our model for practical applications in mineralogy and remote sens-

Table 5. Performance evaluation of Optimized 3D-2D CNN against state-of-the-art methods (Deng et al., 2021)

Classe Name	SAM	SPE-MLP	RNN	SAI-MLP	3D-CNN	ASMLP	Our method
Alunite	0.9198	0.9267	0.9464	0.9423	**0.9607**	0.9522	0.9603
Calcite	0.8077	0.8641	0.9043	0.9182	0.9478	0.9543	**0.9728**
Chalcedony	0.7163	0.8957	0.9037	0.9073	0.9339	0.9233	**0.9527**
Halloysite	0.8779	0.8331	0.8956	0.9012	0.9387	**0.9537**	0.9492
Kaolinite	0.8053	0.8357	0.8842	0.8754	0.9090	0.9186	**0.9233**
Montmorillonite	0.7690	0.8021	0.8374	0.8961	0.9291	0.9353	**0.9443**
Muscovite	0.8853	0.9047	0.9507	0.9332	0.9706	0.9679	**0.9809**
Nontronite	0.8144	0.8529	0.8491	0.8669	0.9039	**0.9284**	0.9226
AA	0.8245	0.8644	0.8964	0.9051	0.9367	0.9417	**0.9508**
OA	0.8331	0.8553	0.8909	0.9103	0.9386	0.9467	**0.9573**

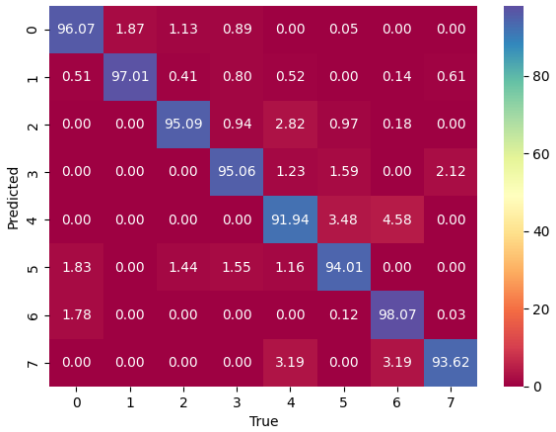

Figure 5. Confusion matrix of our Optimized 3D-2D CNN for mineral classification

ing. More specifically, they indicate high confidence in the model's ability to classify mineral occurrences consistently and accurately. The precision of our model in classifying mineral occurrences is essential for mineral prospecting and geological mapping efforts, as it allows areas of interest to be identified and delineated with a high degree of reliability.

The confusion matrix, as illustrated in Figure 5, offers a comprehensive insight into the performance of our optimized 3D-2D CNN model for mineral classification. It covers a wide range of mineral classes, including: Alunite, Calcite, Chalcedony, Halloysite, Kaolinite, Montmorillonite, Muscovite, and Nontronite; providing a detailed understanding of the model's performance. Examining the diagonal elements representing correct predictions, we observe, generally, high values, indicating a strong performance in classifying instances for each mineral class correctly.

3.3 Comparison with state of the arts

The effectiveness of our 3D-2D CNN, designed for mineral classification from hyperspectral images, is evaluated through a comparative analysis of various classification methods recognized in the specialized literature. SAM method directly measures spectral similarity by calculating the angle between two spectra (Yuhas et al., 1992). The Spectral-Multilayer Perceptron (SPE-MLP) integrates a multilayer perceptron (MLP) that processes the entire spectrum for classification. RNNs analyze spectral sequences in five-point segments, allowing them to capture temporal correlations between samples (Mou et al., 2017). The Spectral Absorption Index-MLP (SAI-MLP) approach uses the SAI vector as input for an MLP (Deng et al., 2021). An improved variant of this method, called Attenuation Spectral Absorption Index-MLP (ASMLP), proposes the construction of an ASAI vector for more efficient extraction of mineral spectral features before its use in an MLP (Deng et al., 2021).

Another method based on a specific type of 3D CNN exploits convolutional neural networks that process three-dimensional data to integrate spatial and spectral attributes of samples (Li et al., 2017). This technique has limitations in fully exploiting the spatial relationships between different spectral bands, which are crucial in hyperspectral imaging. The integration of 2D CNN layers addresses this limitation as regards a full exploitation of the spatial information extracted by the 3D layers. Therefore, the 3D-2D CNN architecture is better suited to capture the complex interplay between spectral and spatial features, leading to a more accurate classification of minerals.

The results in Table 5 show that our optimized 3D-2D CNN outperforms other techniques regarding Overall Accuracy (OA) and Average Accuracy per class (AA), with scores of 95.73% and 95.08%, respectively. This result represents a significant improvement over traditional MLP-based methods such as SPE-MLP and SAI-MLP, as well as the SAM method, which does not involve deep learning. Our optimized CNN demonstrates superiority over advanced techniques such as RNN and standard 3D CNN.

The study shows that combining 3D and 2D methods in CNNs improves classification, especially when hyperspectral data are used. The improvements are illustrated in Table 5: our proposed 3D-2D CNN architecture outperforms the standalone 3D CNN by more than 1.4% in OA and more than 1.85% in AA. These gains highlight the optimized 3D-2D CNN's superior ability to capture the complex interplay between spectral and spatial features.

Choosing a 3D-2D CNN over a 3D CNN alone has significant implications. The results from our comparative analysis show that our optimized model delivers superior classification performance and reduces the computational burden associated with training a 3D CNN model. By leveraging the complementary strengths of 3D and 2D layers, the 3D-2D CNN achieves higher accuracy, making it more effective and efficient. This superiority is evident in the consistent performance gains across different mineral classes, where our model achieves the highest accuracy in most categories.

The improved accuracy achieved by the tour approach underlines its practical value for real-world mineral classification tasks. However, it is crucial to recognize that despite these successes, limitations exist. Optimization of hyperparameters and training on larger, more diverse datasets offer opportunities for model improvement. In addition, exploring adaptations or combinations of our optimized CNN with other deep-learning techniques presents an intriguing direction for tackling specific challenges, such as classifying minerals with almost identical spectral signatures. In conclusion, our optimized 3D-2D CNN sets a new benchmark for automatic mineral classification in hyperspectral imaging. This work creates promising directions for future research and applications in remote sensing.

4 Conclusion

In conclusion, this study successfully implemented an optimized 3D-2D CNN model for automatic mineral classification in hyperspectral images, achieving an impressive accuracy rate of 95.73% on the Cuprite dataset. By integrating the Diagnostic Absorption Band (DAB) selection technique, the model effectively extracted essential spectral features for precise mineral identification. Our model convergence and generalization are improved using learning rate decay and K-fold cross-validation. Comprehensive evaluation metrics, such as AO, Kappa coefficient, and mean accuracy, enabled in-depth assessment of the model's performance. This research provides valuable contributions to mineral classification in hyperspectral imagery, demonstrating the potential of deep-learning models for accurate and reliable mineral detection. Furthermore, future research could explore the application of this model to various hyperspectral datasets and investigate the incorporation of real-time processing capabilities for mineral exploration and environmental monitoring.

References

Beiswenger, T. N., Gallagher, N. B., Myers, T. L., Szecsody, J. E., Tonkyn, R. G., Su, Y.-F., Sweet, L. E., Lewallen, T. A., and Johnson, T. J. (2018). Identification of uranium minerals in natural U-bearing rocks using infrared reflectance spectroscopy. *Applied Spectroscopy*, 72(2):209–224, doi:10.1177/0003702817743326.

Bhatt, D., Patel, C., Talsania, H., Patel, J., Vaghela, R., Pandya, S., Modi, K., and Ghayvat, H. (2021). CNN variants for computer vision: History, architecture, application, challenges and future scope. *Electronics*, 10(20):2470, doi:10.3390/electronics10202470.

Chakraborty, R., Kereszturi, G., Pullanagari, R., Durance, P., Ashraf, S., and Anderson, C. (2022). Mineral prospecting from biogeochemical and geological information using hyperspectral remote sensing – Feasibility and challenges. *Journal of Geochemical Exploration*, 232:106900, doi:10.1016/j.gexplo.2021.106900.

Chang, C.-I. (1999). Spectral information divergence for hyperspectral image analysis. In *IEEE 1999 International Geoscience and Remote Sensing Symposium. IGARSS'99 (Cat. No. 99CH36293)*, volume 1, pages 509–511. IEEE, doi:10.1109/IGARSS.1999.773549.

De Carvalho, O. A. and Meneses, P. R. (2000). Spectral correlation mapper (SCM): An improvement on the spectral angle mapper (SAM). In *Summaries of the 9th JPL Airborne Earth Science Workshop, JPL Publication 00-18*, volume 9, page 2. JPL publication Pasadena, CA, USA.

Deng, K., Zhao, H., Li, N., and Wei, W. (2021). Identification of minerals in hyperspectral imagery based on the attenuation spectral absorption index vector using a multilayer perceptron. *Remote Sensing Letters*, 12(5):449–458, doi:10.1080/2150704X.2021.1903612.

Dennison, P. E., Halligan, K. Q., and Roberts, D. A. (2004). A comparison of error metrics and constraints for multiple endmember spectral mixture analysis and spectral angle mapper. *Remote Sensing of Environment*, 93(3):359–367, doi:10.1016/j.rse.2004.07.013.

El Rahman, S. A. (2016). Hyperspectral image classification using unsupervised algorithms. *International Journal of Advanced Computer Science and Applications*, 7(4).

Farhadi, Z., Bevrani, H., and Feizi-Derakhshi, M.-R. (2022). Combining regularization and dropout techniques for deep convolutional neural network. In *2022 global energy conference (GEC)*, pages 335–339. IEEE, doi:10.1109/GEC55014.2022.9986657.

Fırat, H., Asker, M. E., and Hanbay, D. (2022). Classification of hyperspectral remote sensing images using different dimension reduction methods with 3D/2D CNN. *Remote Sensing Applications: Society and Environment*, 25:100694, doi:10.1016/j.rsase.2022.100694.

Ghaderizadeh, S., Abbasi-Moghadam, D., Sharifi, A., Zhao, N., and Tariq, A. (2021). Hyperspectral image classification using a hybrid 3D-2D convolutional neural networks. *IEEE Journal of Selected Topics in Applied Earth Observations and Remote Sensing*, 14:7570–7588, doi:10.1109/JSTARS.2021.3099118.

Gu, J., Wang, Z., Kuen, J., Ma, L., Shahroudy, A., Shuai, B., Liu, T., Wang, X., Wang, G., Cai, J., and Chen, T. (2018). Recent advances in convolutional neural networks. *Pattern recognition*, 77:354–377, doi:10.1016/j.patcog.2017.10.013.

Hecker, C., van Ruitenbeek, F. J., van der Werff, H. M., Bakker, W. H., Hewson, R. D., and van der Meer, F. D. (2019). Spectral absorption feature analysis for finding ore: A tutorial on using the method in geological remote sensing. *IEEE geoscience and remote sensing magazine*, 7(2):51–71, doi:10.1109/MGRS.2019.2899193.

Ige, A. O. and Sibiya, M. (2024). State-of-the-art in 1D Convolutional Neural Networks: A survey. *IEEE Access*, pages 144082–144105, doi:10.1109/ACCESS.2024.3433513.

Jung, W., Jung, D., Kim, B., Lee, S., Rhee, W., and Ahn, J. H. (2019). Restructuring batch normalization to accelerate CNN training. *Proceedings of Machine Learning and Systems*, 1:14–26.

Kong, F., Hu, K., Li, Y., Li, D., Liu, X., and Durrani, T. S. (2022). A spectral-spatial feature extraction method with polydirectional CNN for multispectral image compression. *IEEE Journal of Selected Topics in Applied Earth Observations and Remote Sensing*, 15:2745–2758, doi:10.1109/JSTARS.2022.3158281.

Kozoderov, V., Kondranin, T., Dmitriev, E., and Kamentsev, V. (2015). Bayesian classifier applications of airborne hyperspectral imagery processing for forested areas. *Advances in Space Research*, 55(11):2657–2667, doi:10.1016/j.asr.2015.02.015.

Kumar, S., Gautam, G., and Saha, S. (2015). Hyperspectral remote sensing data derived spectral indices in characterizing salt-affected soils: A case study of Indo-Gangetic plains of India. *Environmental Earth Sciences*, 73:3299–3308, doi:10.1007/s12665-014-3613-y.

Langley, P., Iba, W., and Thompson, K. (1992). An analysis of Bayesian classifiers. In *Proceedings of the Tenth National Conference of Artificial Intelligence*, volume 90, pages 223–228.

Laukamp, C., Rodger, A., LeGras, M., Lampinen, H., Lau, I. C., Pejcic, B., Stromberg, J., Francis, N., and Ramanaidou, E. (2021). Mineral physicochemistry underlying feature-based extraction of mineral abundance and composition from shortwave, mid and thermal infrared reflectance spectra. *Minerals*, 11(4):347, doi:10.3390/min11040347.

Li, Q. and Niu, C. (2015). Feature-enhanced spectral similarity measure for the analysis of hyperspectral imagery. *Journal of Applied Remote Sensing*, 9(1):096008–096008, doi:10.1117/1.JRS.9.096008.

Li, Y., Zhang, H., and Shen, Q. (2017). Spectral-spatial classification of hyperspectral imagery with 3D convolutional neural network. *Remote Sensing*, 9(1):67, doi:10.3390/rs9010067.

Ma, X., Man, Q., Yang, X., Dong, P., Yang, Z., Wu, J., and Liu, C. (2023). Urban feature extraction within a complex urban area with an improved 3D-CNN using airborne hyperspectral data. *Remote Sensing*, 15(4):992, doi:10.3390/rs15040992.

Mahlein, A.-K., Rumpf, T., Welke, P., Dehne, H.-W., Plümer, L., Steiner, U., and Oerke, E.-C. (2013). Development of spectral indices for detecting and identifying plant diseases. *Remote Sensing of Environment*, 128:21–30, doi:10.1016/j.rse.2012.09.019.

McHugh, M. L. (2012). Interrater reliability: The kappa statistic. *Biochemia medica*, 22(3):276–282.

Mou, L., Ghamisi, P., and Zhu, X. X. (2017). Deep recurrent neural networks for hyperspectral image classification. *IEEE Transactions on Geoscience and Remote Sensing*, 55(7):3639–3655, doi:10.1109/TGRS.2016.2636241.

Ozdemir, A. and Polat, K. (2020). Deep learning applications for hyperspectral imaging: A systematic review. *Journal of the Institute of Electronics and Computer*, 2(1):39–56,

doi:10.33969/JIEC.2020.21004.

Peyghambari, S. and Zhang, Y. (2021). Hyperspectral remote sensing in lithological mapping, mineral exploration, and environmental geology: An updated review. *Journal of Applied Remote Sensing*, 15(3):031501–031501, doi:10.1117/1.JRS.15.031501.

Ranjan, S., Nayak, D. R., Kumar, K. S., Dash, R., and Majhi, B. (2017). Hyperspectral image classification: A k-means clustering based approach. In *2017 4th International Conference on Advanced Computing and Communication Systems (ICACCS)*, pages 1–7. IEEE, doi:10.1109/ICACCS.2017.8014707.

Rao, M., Tang, P., and Zhang, Z. (2019). Spatial-spectral relation network for hyperspectral image classification with limited training samples. *IEEE Journal of Selected Topics in Applied Earth Observations and Remote Sensing*, 12(12):5086–5100, doi:10.1109/JSTARS.2019.2957047.

Roy, S. K., Krishna, G., Dubey, S. R., and Chaudhuri, B. B. (2019). HybridSN: Exploring 3-D–2-D CNN feature hierarchy for hyperspectral image classification. *IEEE Geoscience and Remote Sensing Letters*, 17(2):277–281, doi:10.1109/LGRS.2019.2918719.

Story, M. and Congalton, R. G. (1986). Accuracy assessment: A user's perspective. *Photogrammetric Engineering and remote sensing*, 52(3):397–399.

Swayze, G. A., Clark, R. N., Goetz, A. F., Livo, K. E., Breit, G. N., Kruse, F. A., Sutley, S. J., Snee, L. W., Lowers, H. A., Post, J. L., Stoffregen, R. E., and Ashley, R. P. (2014). Mapping advanced argillic alteration at Cuprite, Nevada, using imaging spectroscopy. *Economic geology*, 109(5):1179–1221, doi:10.2113/econgeo.109.5.1179.

Tripathi, M. K. and Govil, H. (2019). Evaluation of AVIRIS-NG hyperspectral images for mineral identification and mapping. *Heliyon*, 5(11), doi:10.1016/j.heliyon.2019.e02931.

Van der Meer, F. D., Van der Werff, H. M., Van Ruitenbeek, F. J., Hecker, C. A., Bakker, W. H., Noomen, M. F., Van Der Meijde, M., Carranza, E. J. M., De Smeth, J. B., and Woldai, T. (2012). Multi- and hyperspectral geologic remote sensing: A review. *International journal of applied Earth observation and geoinformation*, 14(1):112–128, doi:10.1016/j.jag.2011.08.002.

Wu, H. and Gu, X. (2015). Towards dropout training for convolutional neural networks. *Neural Networks*, 71:1–10, doi:10.1016/j.neunet.2015.07.007.

Xing, Y. and Gomez, R. B. (2001). Hyperspectral image analysis using ENVI (environment for visualizing images). In *Geo-Spatial Image and Data Exploitation II*, volume 4383, pages 79–86. SPIE, doi:10.1117/12.428244.

Yuhas, R. H., Goetz, A. F., and Boardman, J. W. (1992). Discrimination among semi-arid landscape endmembers using the spectral angle mapper (SAM) algorithm. In *JPL, Summaries of the Third Annual JPL Airborne Geoscience Workshop. Volume 1: AVIRIS Workshop*.

Zhang, C., Yi, M., Ye, F., Xu, Q., Li, X., and Gan, Q. (2022). Application and evaluation of deep neural networks for airborne hyperspectral remote sensing mineral mapping: A case study of the Baiyanghe uranium deposit in northwestern Xinjiang, China. *Remote Sensing*, 14(20):5122, doi:10.3390/rs14205122.